INTERNATIONAL JOURNAL OF REMOTE SENSING
2020, VOL. 41, NO. 20, 7931–7957
https://doi.org/10.1080/01431161.2020.1766151

Taylor & Francis
Taylor & Francis Group

Consistent retrieval of multiple parameters from GOES-R top of atmosphere reflectance data

Hengbin Xiong, Hanyu Shi and Zhiqiang Xiao

State Key Laboratory of Remote Sensing Science, Faculty of Geographical Science, Beijing Normal University, Beijing, China

ABSTRACT

Current remote sensing products are mainly generated from polar-orbiting satellite data using parameter-specific algorithms. These products lack physical consistency and cannot accurately characterize intra-day variations of parameters, such as the fraction of absorbed photosynthetically active radiation (FAPAR) and surface albedo. In this study, a multi-parameter consistent retrieval method is proposed to simultaneously retrieve aerosol optical depth (AOD), leaf area index (LAI), photosynthetically active radiation (PAR), FAPAR, surface albedo, and incident shortwave radiation (ISR) from top of atmosphere (TOA) reflectance data acquired by the Advanced Baseline Imager (ABI) aboard the Geostationary Operational Environmental Satellite-R series (GOES-R). The retrieved parameter values were evaluated through comparisons with corresponding Moderate Resolution Imaging Spectroradiometer (MODIS), the second version of the Geoland2 (GEOV2), and GOES-R products and ground measurements over five surface radiation budget network (SURFRAD) sites with different vegetation types. The results demonstrate that the retrieved AOD, PAR, ISR, and surface albedo values have consistent intra-day variations with the ground measurements, and the retrieved parameter values achieve good performance against the ground measurements for all the five SURFRAD sites. The root mean square errors of the retrieved AOD, shortwave albedo, ISR, and PAR values against the ground measurements are 0.071, 0.032, 50.943 W m^{-2}, and 27.975 W m^{-2}, respectively.

ARTICLE HISTORY
Received 14 January 2020
Accepted 13 April 2020

1. Introduction

In order to monitor the status of terrestrial, oceanic, and atmospheric resources on a global scale, a variety of satellites were launched. These satellites can be divided approximately into two categories: polar-orbiting satellites and geostationary satellites. Common polar-orbiting satellites include Terra equipped with Moderate Resolution Imaging Spectroradiometer (MODIS) (Salomonson et al. 1989), National Oceanic and Atmospheric Administration (NOAA) Polar-Orbiting Environmental Satellite (POES) equipped with Advanced Very High Resolution Radiometer (AVHRR) (Townshend 2007), Landsat equipped with Multi-spectral Scanner (MSS)/Thematic Mapper (TM)/Enhanced

CONTACT Zhiqiang Xiao zhqxiao@bnu.edu.cn State Key Laboratory of Remote Sensing Science, Faculty of Geographical Science, Beijing Normal University, Beijing 100875, China

Thematic Mapper Plus (ETM+)/Operational Land Imager (OLI), SPOT equipped with high-resolution visible (HRV)/high-resolution visible and infrared (HRVLR)/VEGETATION (Henry et al. 1996), Environmental Satellite (ENVISAT) equipped with Medium Resolution Imaging Spectroradiometer (MERIS), and Advanced Earth Observation Satellite (ADEOS) equipped with Polarization and Directionality of the Earth's Reflectances (POLDER). Representative geostationary satellites mainly include Himawari-8 equipped with Advanced Himawari Imager (AHI) (Bessho et al. 2016), Geostationary Operational Environmental Satellite-R (GOES-R) equipped with Advanced Baseline Imager (ABI) (Schmit et al. 2008), and Communication, Ocean and Meteorological Satellite (COMS) equipped with Geostationary Ocean Colour Imager (GOCI). The sensors carried by these polar-orbiting and geostationary satellites have acquired a large amount of Earth observation data, which makes it possible to obtain remote sensing parameter products on a global scale.

Currently, various remote sensing products were generated from satellite observations. The National Aeronautics and Space Administration (NASA) produced a series of parameter products, including aerosol optical depth (AOD), leaf area index (LAI), the fraction of absorbed photosynthetically active radiation (FAPAR), surface reflectance, and surface albedo, from MODIS observations. To date, the MODIS series products provide the widest range of applications. The Centre for Global Change Data Processing and Analysis of Beijing Normal University produced the Global Land Surface Satellite (GLASS) products, including LAI, surface albedo, broadband emissivity, photosynthetically active radiation (PAR) and incident shortwave radiation (ISR), from MODIS, AVHRR, and geostationary satellite data (Liang et al. 2013). There are also many similar products such as GEOV1/2 and CYCLOPES LAI, FAPAR, and FCOVER products retrieved from SPOT/VEGETATION observations (Baret et al. 2007, 2013); GIMMS3 g LAI and FAPAR products generated from GIMMS NDVI3 g (Zhu et al. 2013), and the NOAA's National Centres for Environmental Information (NCEI) LAI and FAPAR products derived from the NOAA AVHRR Surface Reflectance data (Claverie, Vermote, and Program 2014).

Although the quality of these parameter products has been hugely enhanced over previous versions, some problems still exist. Current parameter products are separately retrieved from different satellite observations by using the parameter-specific methods, which leads to physical inconsistency among them. Therefore, some studies have attempted to estimate multiple parameters simultaneously with the same physical model and assumptions. Xiao et al. (2015) proposed a data assimilation framework to simultaneously retrieve LAI, FAPAR, and surface albedo from MODIS time-series surface reflectance data. However, complex atmospheric corrections are required to produce surface reflectance data from top of atmosphere (TOA) satellite observations. To avoid the source of some errors caused by atmospheric correction, some methods were developed to estimate remote sensing parameters directly from TOA reflectance data. Lauvernet et al. (2008) used a surface-atmosphere radiative transfer coupled models (PROSPECT+ SAIL+ SMAC) to retrieve AOD, LAI, LAI $\times$ C_{ab} (chlorophyll a and b), and average leaf angle (ALA) from MERIS TOA reflectance data by exploiting spatial and temporal constraints. Shi et al. (2016) utilized a soil-canopy-atmosphere radiative transfer coupled model (ACRM+6 S) to simultaneously estimate LAI, AOD, PAR, FAPAR, surface albedo, and surface reflectance from MODIS TOA reflectance data. By using the same radiative transfer models, physical consistency among the retrieved parameters is ensured.

The above work mainly used polar-orbiting satellite data to retrieve remote sensing parameters. However, many parameters such as AOD, PAR, ISR, and surface albedo have obvious intra-day variations. The parameter products generated from the polar-orbiting satellite data are insufficient if the intra-day variations of these parameters are required. Compared to polar-orbiting satellites, geostationary satellites are able to provide hourly or even higher-frequency observations. Therefore, some methods were developed to estimate remote sensing parameters from geostationary satellite data. Zhang et al. (2011) used a modified Multi-Angle Implementation of Atmospheric Correction (MAIAC) approach to estimate AOD from GOES-12 satellite data. This method can obtain values with a half-hourly temporal resolution. Zhang et al. (2013) developed a 'hybrid' method for consistent AOD retrievals from GOES-East and GOES-West TOA reflectance data.

In addition to the GOES series of geostationary satellite data, other geostationary satellite data, such as MSG/SEVIRI, GOCI, GEMS, and Himawari-8/AHI, have been also used to retrieve remote sensing parameters. Mei et al. (2012) developed an approach for synergistic estimation of AOD and surface reflectance from MSG/SEVIRI data. The retrieved AOD values have a high correlation coefficient with ground measurements from 42 Aerosol Robotic Network (AERONET) sites. Lee et al. (2010) developed a method to estimate aerosol types, AOD, and fine-mode fraction (FMF) with a spatial resolution of 500 m over clear water from GOCI data. This method showed reliable AOD retrievals compared with the MODIS collection 5 and AERONET AOD. Kim et al. (2018) developed an optimal estimation-based algorithm to retrieve AOD and single scattering albedo (SSA) simultaneously from ultraviolet to visible data, which acquired by the Geostationary Environment Monitoring Spectrometer (GEMS) over Asia. Based on aerosol models and band relationships between visible and shortwave infrared (SWIR) channels, Zhang, Hui, and Zheng (2018) proposed an algorithm to retrieve AOD over East Asia with high temporal resolution from Himawari-8/AHI data. The AOD retrievals are able to provide a reference for monitoring the variation of aerosols and forecasting air quality at an hourly scale. Shi et al. (2018) proposed an N-Dimensional Cost Function (NDCF) method to derive the synergistic retrieval of AOD at multiple time points from Himawari-8/AHI image data. This method used a flexible number of observations, took the bidirectional reflectance effect into consideration, and retrieved AOD with a half-hourly temporal resolution.

The studies above have greatly improved the temporal resolution of estimations by using geostationary satellite data. However, these methods mainly focus on estimating AOD. Currently, there are few studies on retrieving multiple parameters with intra-day changes from geostationary satellite data. This paper develops a new method to simultaneously estimate AOD, LAI, ISR, PAR, FAPAR, and surface albedo values with a higher temporal resolution up to 5 minutes from GOES-R TOA reflectance data. The superior temporal resolution enables the study of the intra-day changes of several parameters.

The structure of this paper is as follows: Section 2 introduces the method for surface and atmospheric parameter retrieval. The data used in this study (including GOES-R TOA reflectance data, satellite products for comparisons and ground measurements) are also introduced in this section. Section 3 shows the retrieval results, which are evaluated with ground measurements and existing products over the five selected sites. Section 4 provides conclusions and discussion.

2. Methodology and data

In the study, we developed a consistent retrieval method to simultaneously estimate multiple parameters from GOES-R TOA reflectance data. A soil-canopy-atmosphere radiative transfer coupled model is used to simulate TOA reflectance under a clear sky. The GOES-R TOA reflectance with cloud are screened out by the Savitzky-Golay filtering algorithm. The GLASS LAI and MERRA-2 AOD products are utilized to provide prior LAI and AOD values. A cost function, defined as the sum of the squares of the distances between the simulated TOA reflectance and the GOES-R TOA reflectance with the highest quality plus the squares of the distances between the control variables and the corresponding prior values, is constructed. Next, a global optimization method is applied to search the optimal estimates of LAI and AOD that minimizes the cost function. Then, the optimal estimates are input into the soil-canopy-atmosphere radiative transfer coupled model to calculate ISR, PAR, FAPAR, shortwave albedo, and visible albedo values. Figure 1 shows a flowchart for the consistent retrieval of multiple parameters from GOES-R TOA reflectance data.

2.1. The soil-canopy-atmosphere radiative transfer coupled model

The soil-canopy-atmosphere radiative transfer coupled model developed by Shi et al. (2016) was used to simulate TOA reflectance. It coupled a two-layer canopy reflectance model (ACRM) with the Second Simulation of the Satellite Signal in the Solar Spectrum (6 S) model on the basis of the four-stream theory (Verhoef 1985). The ACRM coupled PROSPECT with a soil model. PROSPECT is a leaf optical properties model, which can simulate transmittance and reflectance of various plant leaves (Jacquemoud and Baret 1990). The soil model, developed by Walthall et al. (1985), can simulate bidirectional reflectance of soil surfaces. The ACRM can simulate canopy reflectance in the wavelength range from 400 to 2400 nm for arbitrary observation geometry (Kuusk 2001).

The 6 S model is suitable for the simulation of the atmospheric radiative transfer process in the solar spectral range of 0.25 to 4 μm under clear-sky conditions (Vermote et al. 2006). In order to speed up the simulation, a look-up table (LUT) is generated. Path reflectance, atmospheric transmittance, and spherical albedo for the selected bands of GOES-R ABI were calculated under various atmospheric conditions and different geometries within a certain range: solar zenith angle and view zenith angle for 0° to 70° at 5° intervals; relative azimuth angle for 0° to 180° at 30° intervals; elevation for 0 to 3 km at 0.5 km intervals; five predefined aerosol types of the 6 S model; and AOD of 550 nm for 0.0 to 1.0 at a 0.05 interval.

Taking the multiple scattering among soil, canopy, and atmosphere media into consideration, the TOA reflectance, r_{TOA}, can be expressed by the following general formula (Verhoef 1985; Verhoef and Bach 2003; Shi et al. 2016):

$$r_{TOA} = \rho_{so} + \tau_{ss} r_{so} \tau_{oo} + \frac{(\tau_{ss} r_{sd} + \tau_{sd} r_{dd}) \tau_{do} + (\tau_{sd} + \tau_{ss} r_{sd} \rho_{dd}) r_{do} \tau_{oo}}{1 - r_{dd} \rho_{dd}} \quad (1)$$

where r_{so} is the bi-directional reflectance at top of the canopy (TOC), r_{sd} is the directional-hemispherical reflectance at TOC, r_{do} is the hemispherical-directional reflectance at TOC, and r_{dd} is the bi-hemispherical reflectance at TOC, ρ_{so} is the atmospheric bi-directional

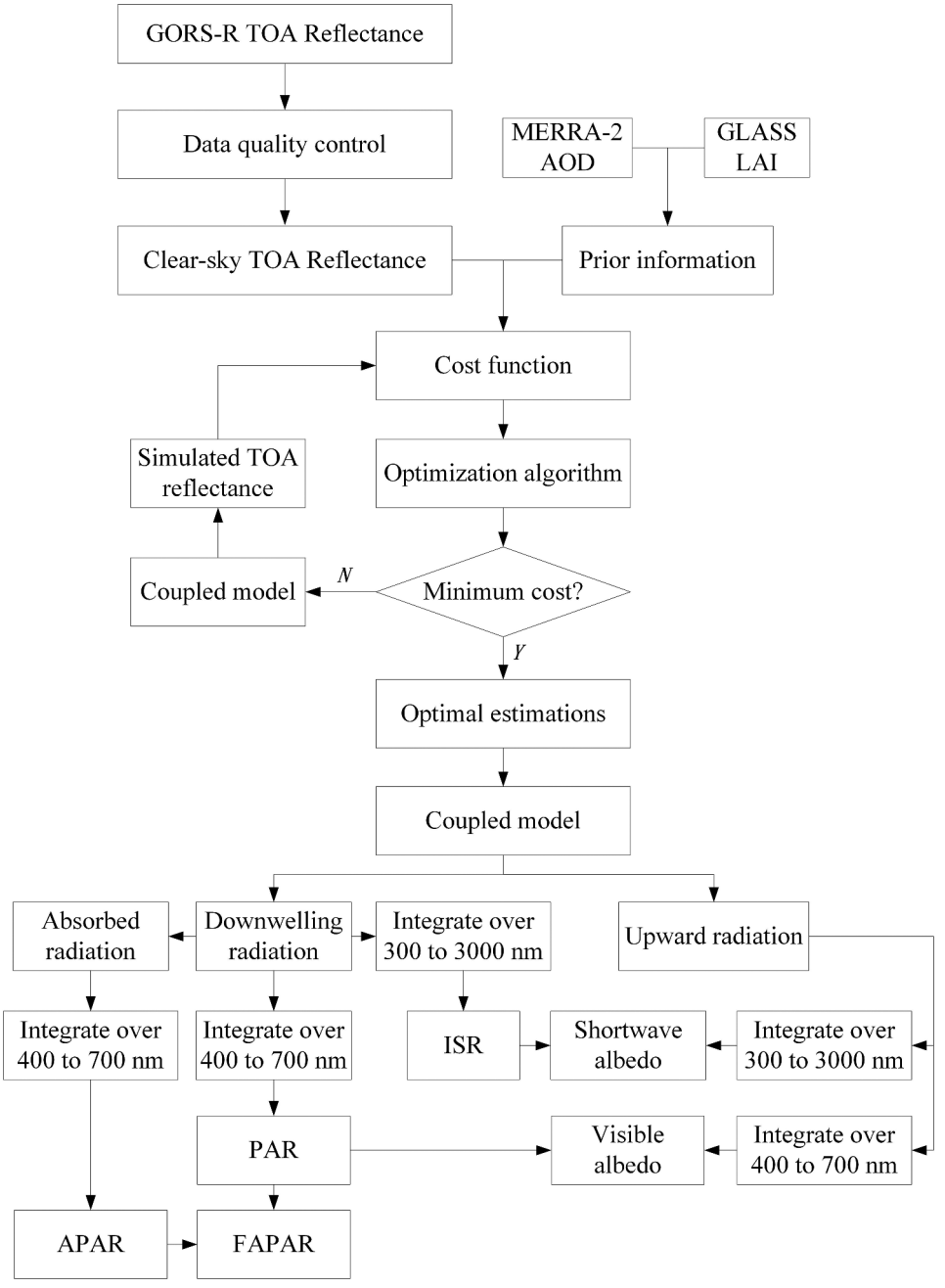

Figure 1. Flowchart for the consistent retrieval of multi-parameters from GOES-R TOA reflectance data.

reflectance at TOA, and ρ_{dd} is the atmospheric bi-hemispherical reflectance at bottom of atmosphere, τ_{sd} is the diffuse atmospheric transmittance for solar incidence, τ_{do} is the directional atmospheric transmittance for diffuse incidence, τ_{ss} and τ_{oo} are the direct atmospheric transmittances in the direction of solar incidence and the observation direction, respectively.

Table 1. Parameters for the coupled soil-canopy-atmosphere radiative transfer model.

Parameter name	Symbol	Range	Unit
Aerosol optical depth at 550 nm*	AOD	0.0 to 1.0	–
Leaf area index*	LAI	0 to 10.0	$m^2\ m^{-2}$
Leaf specific weight*	SLW	40.0 to 200.0	$g\ m^{-2}$
Leaf water content*	c_1	80.0 to 180.0	% of SLW
Chlorophyll AB content*	c_2	0.2 to 0.7	% of SLW
Leaf dry matter content	c_3	98.0	% of SLW
Anthocyanin	c_4	0.038	% of SLW
Leaf structure parameter	l_s	1.624	–
Weight of the first Price function*	s_1	0.05 to 0.4	–
Weight of the second Price function	s_2	0.0	–
Weight of the third Price function	s_3	0.0	–
Weight of the fourth Price function	s_4	0.0	–
Hot-spot parameter	h_s	0.1	–
Foliage clumping parameter	CI	0.4 to 1.2	–
Displacement parameter	s_{zz}	1.2	–
Elliptical leaf angle distribution	e_{ln}	2.0	–
Modal leaf angle	t_{hm}	75.0	°
Refraction index factor	n_{ratio}	0.9	–

Table 2. The selected four bands of the GOES-R ABI sensor.

ABI channel	Band type	Wavelength range (μm)	Spatial resolution at nadir (km)
1	Blue	0.45 to 0.49	1.0
2	Red	0.59 to 0.69	0.5
3	NIR	0.85 to 0.88	1.0
5	SWIR	1.58 to 1.64	1.0

Table 1 lists all of the input parameters of the coupled model. A global sensitivity analysis for the selected GOES-R bands indicates that LAI, AOD, leaf water content (c_1), chlorophyll AB content (c_2), leaf specific weight (SLW), and weight of the first Price function (s_1) are the most sensitive parameters of the coupled model. These parameters were identified as control variables and marked by an asterisk in Table 1. In this study, the foliage clumping parameter (CI) was set to averages of the clumping index values from the global clumping index product generated by Jiao et al. (2014), Jiao et al. (2016, 2018) and Dong et al. (2018), and other parameters of the coupled model were set to default values.

2.2. Retrieval process of parameters

In this paper, a cost function is constructed to retrieve the optimal values of the control variables from cloud-free GOES-R TOA reflectance data. The form of the cost function can be expressed as

$$J(\boldsymbol{X}) = \frac{1}{2}(\boldsymbol{H}(\boldsymbol{X}) - \boldsymbol{Y}_o)^T \mathbf{O}^{-1}(\boldsymbol{H}(\boldsymbol{X}) - \boldsymbol{Y}_o) + \frac{1}{2}(\boldsymbol{X} - \boldsymbol{X}_p)^T \mathbf{C}^{-1}(\boldsymbol{X} - \boldsymbol{X}_p) \quad (2)$$

where $\boldsymbol{X} = [\mathrm{AOD}, \mathrm{LAI}, \mathrm{SLW}, c_1, c_2, s_1]^T$ is the vector of the control variables, vector $\boldsymbol{X}_p$ represents the prior values corresponding to the control variables, vector $\boldsymbol{Y}_o$ represents the GOES-R TOA reflectance including four bands, and $\boldsymbol{H}(\boldsymbol{X})$ is the vector of TOA reflectance simulated by the coupled model for the corresponding bands. Matrix **O** represents

the error covariance of GOES-R TOA reflectance and matrix **C** represents the error covariance of the prior information. In this study, the diagonal error covariance matrices were used. The uncertainty of the GOES-R TOA reflectance for each band is obtained by 0.05 times the TOA reflectance of the corresponding bands. The uncertainty of AOD is calculated by 0.2 × AOD + 0.05 (Kaufman et al. 1997). The uncertainty of LAI is set to the standard deviations of the GLASS LAI product from 2000 to 2017.

The SCE-UA method was chosen to find the optimal values of the control variables by minimizing the cost function. The SCE-UA method is a robust global optimization method. It has a lower dependence on the initial values of parameters compared to other optimization methods (Duan, Gupta, and Sorooshian 1993).

After the optimal values of the control variables were obtained, they were input into the coupled model to calculate ISR, PAR, FAPAR, visible and shortwave albedo values. ISR is the sum of the incident solar radiation on the Earth's surface in the range of 300 to 3000 nm and can be expressed as

$$\mathrm{ISR} = \int_{300}^{3000} \left\{ E_{\mathrm{Sun}}(\lambda) + E_{\mathrm{Sky}}(\lambda) \right\} \mathrm{d}\lambda \tag{3}$$

where E_{Sun} and E_{Sky} are direct and sky irradiance at the Earth's surface, respectively.

PAR is the incident shortwave radiation in the 400 to 700 nm range and can be expressed as

$$\mathrm{PAR} = \int_{400}^{700} \left\{ E_{\mathrm{Sun}}(\lambda) + E_{\mathrm{Sky}}(\lambda) \right\} \mathrm{d}\lambda \tag{4}$$

APAR is defined as the solar radiation in the range of 400 to 700 nm that is absorbed by the vegetation, which can be written as

$$\mathrm{APAR} = \int_{400}^{700} \left\{ E_{\mathrm{Sun}}(\lambda) \alpha_{\mathrm{s}}^{*} + E_{\mathrm{Sky}}(\lambda) \alpha_{\mathrm{d}}^{*} \right\} \mathrm{d}\lambda \tag{5}$$

where α_{s}^{*} and α_{d}^{*} are canopy absorptance for direct and hemispherical diffuse incident flux, respectively. A detailed calculation formula for these two parameters can be found in (Verhoef and Bach 2007).

FAPAR is the proportion of PAR that is absorbed by vegetation. It can be calculated by Equation (6):

$$\mathrm{FAPAR} = \frac{\mathrm{APAR}}{\mathrm{PAR}} \tag{6}$$

Surface albedo is the ratio of upward to downward solar radiation at the Earth's surface. Broadband albedo with a range of 300 to 3000 nm is called shortwave albedo, while visible albedo occurs within a range of 400 to 700 nm. The shortwave and visible albedo, denoted by A_{sw} and A_{vis}, respectively, can be calculated as follows:

$$A_{\mathrm{sw}} = \frac{\int_{300}^{3000} \left\{ E_{\mathrm{Sun}}(\lambda) r_{\mathrm{sd}} + E_{\mathrm{Sky}}(\lambda) r_{\mathrm{dd}} \right\} \mathrm{d}\lambda}{\int_{300}^{3000} \left\{ E_{\mathrm{Sun}}(\lambda) + E_{\mathrm{Sky}}(\lambda) \right\} \mathrm{d}\lambda} \tag{7}$$

and

$$A_{vis} = \frac{\int_{400}^{700} \{E_{Sun}(\lambda) r_{sd} + E_{Sky}(\lambda) r_{dd}\} d\lambda}{\int_{400}^{700} \{E_{Sun}(\lambda) + E_{Sky}(\lambda)\} d\lambda} \quad (8)$$

A detailed calculation of each parameter can be found in (Verhoef and Bach 2003) and (Shi et al. 2016).

2.3. Evaluation metrics for retrieved parameters

The performance of the retrieved parameters was evaluated based on three indicators, including the root mean square error (RMSE), Bias, and coefficient of determination (R^2). These indicators have been widely used in assessing the performances of remote sensing parameter products. The RMSE, Bias, and R^2 can be calculated as follows:

$$\text{RMSE} = \sqrt{\frac{1}{N}\sum_{i=1}^{N}(v_i - g_i)^2} \quad (9)$$

$$\text{Bias} = \frac{1}{N}\sum_{i=1}^{N}(v_i - g_i) \quad (10)$$

$$\text{R}^2 = 1 - \frac{\sum_{i=1}^{N}(v_i - g_i)^2}{\sum_{i=1}^{N}(v_i - \bar{v})^2} \quad (11)$$

where v_i is the i-th retrieved value for the parameter being evaluated, g_i is the corresponding ground measurement, $\bar{v}$ is the mean of v_i, and N is the total number of ground measurements.

2.4. Data

2.4.1. GOES-R data

GOES-R is the designated GOES-East after substituting GOES-13 on 18 December 2017. The ABI sensor aboard the GOES-R has a total of 16 bands and acquires observations with high spatial and temporal resolutions. The spatial resolution of these data is 0.5 km for the red band (band 2), 1 km for the blue (band 1), near-infrared (NIR) (band 3), and SWIR (band 5) bands, and 2 km for the other 12 bands. The temporal resolution of these data is 5 minutes for the Continental United States (CONUS) and 15 minutes for Full Disk. This study selects the Blue, Red, NIR, and SWIR bands for retrieval of multiple parameters. Detailed information about the four bands is given in Table 2.

Since the 6 S model can only simulate TOA reflectance under clear-sky conditions, a quality control technique developed by Xiao et al. (2011) was applied to select the GOES-R TOA reflectance data with high quality. The GOES-R TOA reflectance data are used to calculate time-series Normalized Different Vegetation Index (NDVI), and a Savitzky-Golay filter is used to calculate upper envelopes of the time-series NDVI. If the NDVI value at the i-th point, $(\text{NDVI})_i$, satisfies the following condition, the corresponding TOA reflectance data are considered to be not contaminated by clouds.

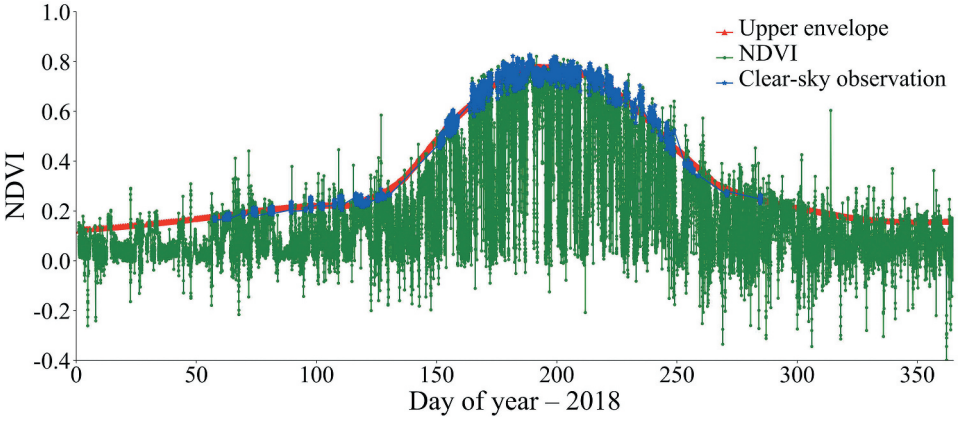

Figure 2. Time-series NDVI to identify clear-sky GOES-R TOA reflectance data at the Bondville site, 2018.

$$\left|(\mathrm{NDVI})_i - (E_{\mathrm{NDVI}})_i\right| < 0.1 \times (E_{\mathrm{NDVI}})_i \tag{12}$$

where $(E_{\mathrm{NDVI}})_i$ is the NDVI value of the upper envelope corresponding to $(\mathrm{NDVI})_i$, and $|\cdot|$ is the absolute operator. In addition, the NDVI should be higher than the 2-band Enhanced Vegetation Index (EVI2) (Jiang et al. 2008) and the TOA reflectance in the NIR band should be less than 0.2. If a TOA reflectance value satisfies the above conditions, it is considered to be cloud-free in this study.

Figure 2 shows the time-series NDVI calculated from GOES-R TOA reflectance and the upper envelopes of the time-series NDVI at the Bondville site in 2018. The blue points are identified as cloud-free observations. Only the cloud-free TOA reflectance data were used in this study.

2.4.2. GLASS LAI and MERRA-2 AOD products

The GLASS LAI and MERRA-2 AOD products were used to provide prior LAI and AOD values, respectively. The GLASS LAI product provides two datasets: GLASS AVHRR and GLASS MODIS. The GLASS AVHRR LAI product was produced from AVHRR data. It has a temporal resolution of 8 days and a spatial resolution of 0.05°, and spans from 1981 to 2018. The GLASS MODIS LAI product was generated by MODIS data. It is provided at a temporal resolution of 8 days and a spatial resolution of 1 km, and spans from 2000 to 2018 (Xiao et al. 2014, 2016). In this study, the averages of the GLASS MODIS LAI product from 2000 to 2017 were used as the prior LAI values.

The MERRA-2 AOD product has a temporal resolution of 1 hour and a spatial resolution of 0.625° × 0.5° (longitude-by-latitude) from 1980 to present (Collow et al. 2017). The MERRA-2 AOD values at the time closest to satellite observations were used as the prior AOD values.

2.4.3. Satellite products for comparisons

In this study, the retrieved parameters were compared with the corresponding MODIS, GEOV2, and GOES-R products. The MODIS and GEOV2 LAI/FAPAR products were used for comparison with the retrieved LAI and FAPAR values. The MODIS LAI/FAPAR products

(MOD15A2 H) have a temporal resolution of 8 days and a spatial resolution of 500 m. The GEOV2 LAI/FAPAR products were generated from daily VEGETATION data by using a neural network algorithm. The temporal and spatial resolutions of the GEOV2 LAI/FAPAR products are 10 days and 1/112° (about 1 km at the Equator), respectively, from 1999 to present. The MODIS visible and shortwave albedo products (MCD43A3) were compared with the retrieved visible and shortwave albedo values. MCD43A3 is available since 2000. It has a spatial resolution of 500 m and a daily temporal resolution (Schaaf and Wang 2015). The GOES-R AOD product was compared with the retrieved AOD values. It has a temporal resolution of 5 minutes and a spatial resolution of 2 km for the CONUS during the daytime (Valenti 2018). The GOES-R AOD product divides the data quality into four levels known as 0-good, 1-medium, 2-low, and 3-not produced. In this study, only the GOES-R AOD values with a good and medium quality were used for comparison with the retrieved AOD values.

2.4.4. Ground measurements

There are seven widely used sites from surface radiation budget network (SURFRAD) for validation (Augustine, DeLuisi, and Long 2000). These sites are Bondville, Goodwin Creek, Penn State, Sioux Falls, Table Mountain, Fort Peck, and Desert Rock. Because there are no high-quality GOES-R AOD data at the Fort Peck site and the Desert Rock site is a desert site, only the ground measurements over the other five SURFRAD sites were used to verify the estimated parameters in this study. Table 3 lists detailed information on the five SURFRAD sites. The Bondville site is located in southwest of Champaign, Illinois. It is an agricultural site for farming soybeans and corn alternately. The Goodwin Creek site, located in west of Oxford, Mississippi, is covered with pastural grass. The Penn State site, located in a wide valley between Tussey and Bald Eagle Ridges, is an agricultural site for research affiliate to Pennsylvania State University (Augustine, DeLuisi, and Long 2000). The Sioux Falls site is located in South Dakota with grass as the characteristic vegetation type. The Table Mountain site, located in Colorado, is mainly covered with sparse grass and desert shrubs with small cacti.

At these SURFRAD sites, there are ground-measured AOD, PAR, ISR, and shortwave albedo with a temporal resolution of 1 minute. The ground-measured AOD values are provided at the following central wavelength with a bandwidth of 10 nm: 415 nm, 500 nm, 615 nm, 673 nm, 870 nm, and 940 nm. In this study, the ground-measured AOD values at 500 nm and the Ångström exponent parameter were used to calculate the AOD values at 550 nm. The ground-measured shortwave albedo is the ratio of upward to downward shortwave radiation. Generally, clouds may affect downward shortwave radiation for a few seconds of time (Long and Ackerman 2000). In order to reduce the systematic error and the possible mismatch of time, the average of the ground-

Table 3. Detailed information on the selected sites.

Site name	Latitude (°)	Longitude (°)	Elevation (m)	Land cover
Bondville	40.0519	− 88.3731	230	Cropland
Goodwin Creek	34.2547	− 89.8729	98	Pasture
Penn State	40.7201	− 77.9309	376	Cropland
Sioux Falls	43.7340	− 96.6233	473	Grassland
Table Mountain	40.1250	− 105.2368	1689	Grassland

measured shortwave albedo values over a time window of 6 minutes was used to validate the retrieved the shortwave albedo values. For the same reason, the retrieved AOD values were validated by the average of the ground-measured AOD values over a time window of 6 minutes.

3. Results

The method developed in this study was tested at the five sites with different vegetation types. For each site, the GOES-R TOA reflectance data in 2018 were used to simultaneously retrieve AOD, LAI, ISR, PAR, FAPAR, and surface albedo. The retrieved results were compared with the MODIS LAI, FAPAR, and surface albedo products, the GEOV2 LAI and FAPAR products, the GEOES-R AOD product and the ground measurements. For each site, time series of the retrieved LAI, FAPAR, ISR, PAR, shortwave albedo, visible albedo, and AOD values were demonstrated. At the same time, time series of the retrieved results on three separate days were also shown to better evaluate intra-day variations of the retrieved parameters. The specific days selected for evaluation were based on the availability of the MODIS, GEOV2, and GEOES-R products and the ground measurements.

Figure 3 demonstrates time-series of the retrieved LAI, FAPAR, ISR, PAR, albedo, and AOD values at the Bondville site. The retrieved parameter values on days 205, 217, and 221 are also shown in Figure 3 to analyse intra-day variations of these parameters at this site. Figure 3(*a*) illustrates the retrieved, GEOV2, and MODIS LAI values. The LAI retrievals are in good agreement with the MODIS LAI values in terms of amplitude before day 180, but the LAI retrievals are higher than the MODIS LAI values for days 190 to 250. The MODIS LAI value reached 6.7 on day 185, which was much larger than the retrieved and GEOV2 LAI values. The GEOV2 LAI values are systematically higher than the retrieved and MODIS LAI values for the whole year. On days 205, 217, and 221, the retrieved LAI values hardly changed within a single day, which is in line with the actual situation. Figure 3(*b*) demonstrates that the FAPAR retrievals are consistent with the MODIS and GEOV2 FAPAR values during the growing season. The GEOV2 FAPAR values are larger than the retrieved and MODIS FAPAR values outside of the time of growing season. The retrieved FAPAR profiles on days 205, 217, and 221 show a concave shape. This is primarily due to changes in the solar zenith angle, which significantly affects the incident amount of PAR and the optical transmission path (Dong et al. 2016). The retrieved FAPAR profiles reach their minimum values near the local solar noon for the sake of the shortest path length from the canopy to the soil (Pinter 1993). Figure 3(c) shows that the ISR retrievals achieved excellent agreement with the ground-measured ISR values, both in terms of magnitude and the pattern of daily changes. Figure 3(d) shows the retrieved PAR values in 2018 and the retrieved PAR profiles on days 205, 217, and 221. Similar to the retrieved ISR values, the retrieved PAR values have similar seasonal and intra-day patterns to the ground-measured PAR values, but they are a bit larger than the ground-measured PAR values at this site. Figure 3(e) demonstrates a comparison of the retrieved shortwave albedo values with the MODIS and ground-measured shortwave albedo values. During the non-growing season, the retrieved values and the MODIS shortwave albedo values are lower than the ground-measured shortwave albedo values. However, the shortwave albedo retrievals are slightly larger than the

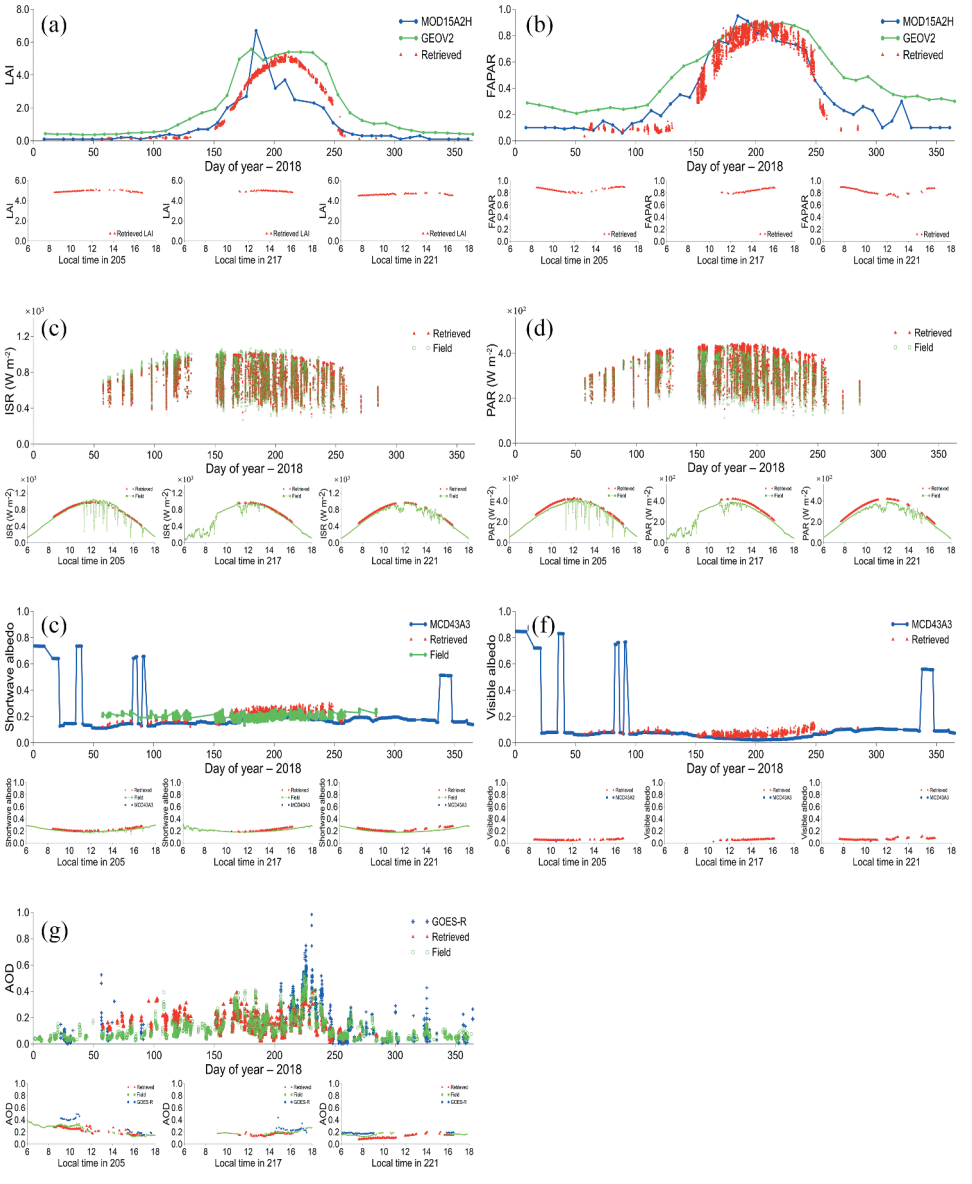

Figure 3. Time series for (*a*) LAI, (*b*) FAPAR, (*c*) ISR, (*d*) PAR, (*e*) shortwave albedo, (*f*) visible albedo, and (*g*) AOD at the Bondville site in 2018.

ground-measured shortwave albedo values during the crop growing season. Figure 3 (f) shows the retrieved values and the MODIS albedo values in the visible bands. Before day 150 and after day 250, the retrieved visible albedo values are in a good agreement with the MODIS visible albedo values. However, the retrieved visible albedo values are a bit larger than the MODIS visible albedo values during the growing season. Compared with the retrieved visible albedo values, the retrieved shortwave albedo values show a large number of obvious intra-day changes at this site. The retrieved shortwave albedo values slowly decrease from morning to noon,

and gradually increase from noon to night within a single day, which is in good agreement with the diurnal variation characteristics of the ground-measured shortwave albedo values for the selected 3 days. Figure 3(g) illustrates that the retrieved values and the GOES-R AOD values fit well with the ground-measured AOD values. On days 205 and 217, the retrieved AOD values are closer to the ground-measured AOD values than the GOES-R AOD values. On day 221, the retrieved AOD values are a bit lower than the ground-measured AOD values, while the GOES-R AOD values are higher than the ground-measured AOD values at this site.

Figure 4 illustrates the scatter density plots of the retrieved AOD, ISR, PAR, and shortwave albedo values versus the ground measurements for the corresponding parameters at the Bondville site. For comparison, the scatter density plots of the GOES-R AOD values and the MODIS shortwave albedo values versus the corresponding ground measurements are also shown in Figure 4. Figure 4(*a*,*b*) shows the scatter density plots of the retrieved values and the GOES-R AOD values versus the ground-measured AOD values, respectively. A good agreement between the retrieved AOD values and the ground-measured AOD values was observed at this site. The GOES-R AOD values overestimated the ground-measured AOD values when the AOD values were high, and underestimated the ground-measured AOD values when the AOD values were low. It is clear from these scatter density plots that the retrieved AOD values achieve better performance (RMSE = 0.073 and Bias = −0.007) against the ground-measured AOD values than the GOES-R AOD values (RMSE = 0.124 and Bias = 0.027) at this site. Figure 4(*c*,*d*) are the scatter density plots of the retrieved ISR and PAR values against the corresponding ground-measured ISR and PAR values, respectively. The retrieved ISR values agree well with the ground-measured ISR values, while the retrieved PAR values were slightly higher than the ground-measured PAR values. There are some scatters

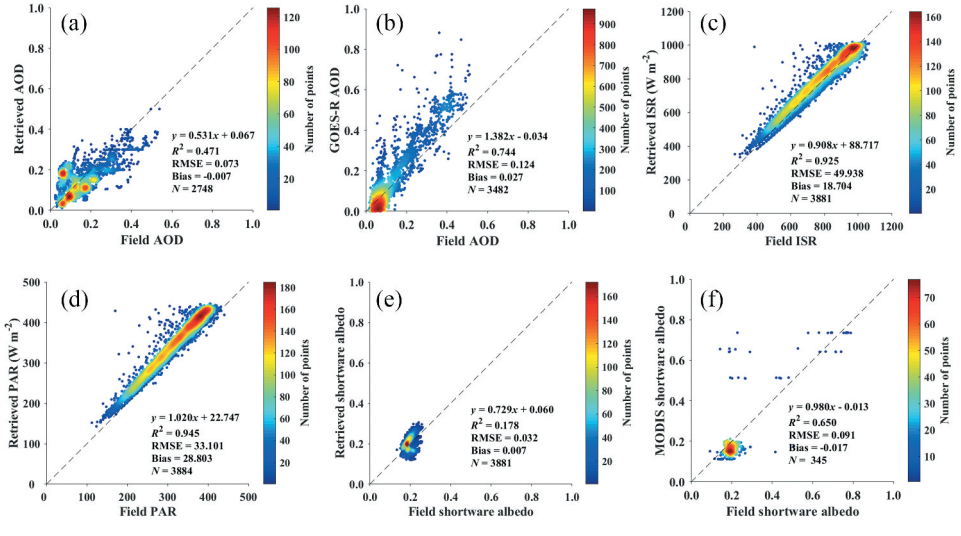

Figure 4. Scatter density plots of (*a*) the retrieved AOD values, (*b*) the GEOES-R AOD values, (*c*) the retrieved ISR values, (*d*) the retrieved PAR values, (*e*) the retrieved shortwave albedo values, and (*f*) the MODIS shortwave albedo values versus the ground measurements of the corresponding parameters at the Bondville site in 2018.

isolated further away from the 1:1 line. The retrieved ISR and PAR values at these scatters are obviously larger than the corresponding ground measurements. This may be caused by a mismatch of time. Figure 4(*e*,*f*) are the scatter density plots of the retrieved values and the MODIS shortwave albedo values versus the ground-measured shortwave albedo values. The scatters for the retrieved values and the MODIS shortwave albedo values are basically clustered in a small, circular area near the 1:1 line. The high shortwave albedo values in Figure 4(f) may be resulted by snow (Wang et al. 2014). By comparison, the retrieved shortwave albedo values provided the better performance (RMSE = 0.032 and Bias = 0.007) than the MODIS shortwave albedo values (RMSE = 0.091 and Bias = −0.017).

Figure 5 illustrates the retrieved results at the Goodwin Creek site in 2018, and the retrieved LAI, FAPAR, ISR, PAR, albedo, and AOD values on days 202, 206, and 223 to analyse any intra-day variations in these parameters. For comparison, the GEOV2 LAI and FAPAR values, the MODIS LAI, FAPAR, and surface albedo values, the GEOES-R AOD values, and the ground measurements for the corresponding parameters at this site are also shown in Figure 5. Figure 5(*a*) shows that the retrieved LAI profile has a similar seasonality pattern with the MODIS and GEOV2 LAI profiles. The retrieved LAI profile is in good agreement with the upper envelope of the time-series MODIS LAI values for the whole year. The GEOV2 LAI values are larger than the retrieved and MODIS LAI values during the most vigorous growth stage, and achieved good agreement with the retrieved and MODIS LAI values during the non-growing season. Figure 5(*b*) illustrates that the FAPAR retrievals fit well with the MODIS and GEOV2 FAPAR in terms of overall change trend and amplitude. The FAPAR retrievals show obvious intra-day variation characteristics on days 202, 206, and 223. The amount of intra-day variation is around 0.2 in 1 day as the solar zenith angle and atmospheric conditions change. The minimum of the retrieved FAPAR values in a day occurs approximately at the local solar noon. Figure 5(*c*,*d*) show the profiles of the retrieved ISR and PAR values, respectively. For comparison, the ground-measured ISR and PAR values are also shown in Figure 5(*c*,*d*). The retrieved ISR values have a similar magnitude and pattern with the ground-measured ISR values both in terms of seasonal and intra-day changes. The retrieved PAR values are a bit larger than the ground-measured PAR values, although the retrieved PAR values have a similar trend with the ground-measured PAR values within the day. The profiles of the retrieved, MODIS, and ground-measured shortwave albedo values are shown in Figure 5(*e*). Before day 150 and within the period of days 240 to 307, the retrieved shortwave albedo values are slightly larger than the ground-measured shortwave albedo values. During the growth stage, the shortwave albedo retrievals achieve excellent agreement with the ground-measured shortwave albedo. The MODIS shortwave albedo values are systematically lower than the ground-measured shortwave albedo values, particularly outside of the time of growth stage at this site. Figure 5(*f*) shows the visible albedo values of the retrieved results and MODIS. As shown in Figure 5(*e*), the MODIS visible albedo values are systematically lower than the retrieved visible albedo values for the whole year. Figure 5(*g*) shows the retrieved AOD values, as well as the GOES-R and ground-measured AOD values for the whole year of 2018. The retrieved AOD values generally agree with the ground-measured AOD values, but the GOES-R AOD shows several high values before day 100. The time series of the AOD values on day 206 demonstrate that the retrieved AOD values are a bit higher than the ground-measured AOD values and are obviously lower than the GOES-R AOD values.

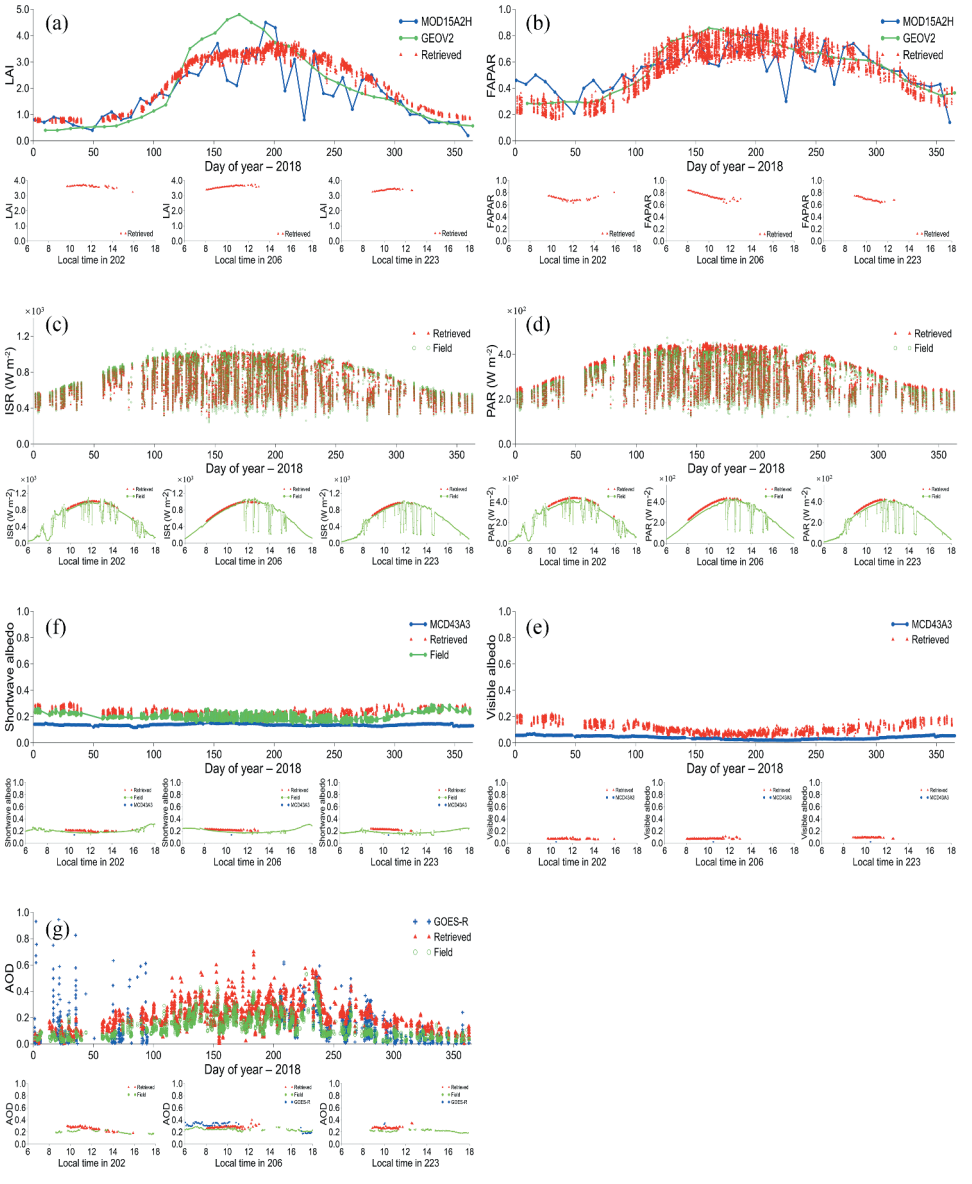

Figure 5. Time series for (*a*) LAI, (*b*) FAPAR, (*c*) ISR, (*d*) PAR, (*e*) shortwave albedo, (*f*) visible albedo, and (*g*) AOD at the Goodwin Creek site in 2018.

Figure 6 shows scatter density plots of the retrieved AOD, ISR, PAR, and shortwave albedo values, as well as the GOES-R AOD values and the MODIS shortwave albedo values, versus the ground measurements of the corresponding parameters at the Goodwin Creek site in 2018. Figure 6(*a*) illustrates that the AOD retrievals are systematically larger than the ground-measured AOD values, manifested as the majority of the scatters concentrated above the 1:1 line. Although the GOES-R AOD values overestimated the ground-measured AOD values when the AOD values were high (shown in Figure 6(*b*)), the GOES-R AOD values outperformed the retrieved AOD values at this site. Figure 6(*c*,*d*) are the

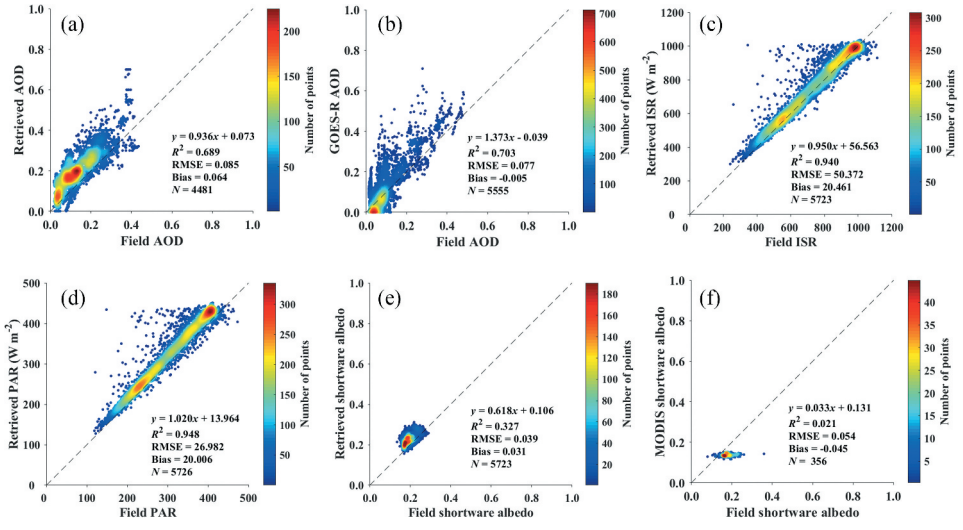

Figure 6. Scatter density plots of (*a*) the retrieved AOD values, (*b*) the GEOES-R AOD values, (*c*) the retrieved ISR values, (*d*) the retrieved PAR values, (*e*) the retrieved shortwave albedo values, and (*f*) the MODIS shortwave albedo values versus the ground measurements of the corresponding parameters at the Goodwin Creek site in 2018.

scatter density plots of the retrieved ISR and PAR values against the ground-measured ISR and PAR values, respectively. The retrieved ISR values agree well with the ground-measured ISR values, whereas the retrieved PAR values are a bit higher than the ground-measured PAR values. Figure 6(*e*,*f*) are the scatter density plots of the retrieved and MODIS shortwave albedo values against the ground-measured shortwave albedo values. At this site, the retrieved results perform better (RMSE = 0.039 and Bias = 0.031) against the ground-measured shortwave albedo values compared to the MODIS shortwave albedo values (RMSE = 0.054 and Bias = −0.045).

Figure 7 illustrates the retrieved LAI, FAPAR, ISR, PAR, albedo, and AOD values at the Penn State site in 2018, as well as the retrieved parameter values on days 227, 236, and 240, to analyse the intra-day variations of these parameters. Figure 7(*a*) illustrates that the retrieved, GEOV2, and MODIS LAI values achieve good agreement during the non-growing season. The profile of the LAI retrievals agrees with the envelope of the time-series MODIS LAI values during the growth stage, but the GEOV2 LAI values are significantly larger than these. Figure 7(*b*) demonstrates that the retrieved, GEOV2, and MODIS FAPAR values have similar seasonal patterns. The retrieved FAPAR values are almost located between the profiles of the MODIS and GEOV2 FAPAR values during the growth stage. The retrieved FAPAR values show obvious intra-day variation characteristics on days 227, 236, and 240, with the amount of intra-day variation greater than 0.4. Figure 7(*c*) demonstrates that the ISR retrievals are in agreement with the ground-measured ISR values for seasonal and intra-day changes. The retrieved PAR values shown in Figure 7(*d*) are a bit larger than the ground-measured PAR values, but have a similar intra-day change pattern with the ground-measured PAR values on days 227, 236, and 240. Figure 7(*e*) illustrates that the retrieved shortwave albedo values perform better than the MODIS

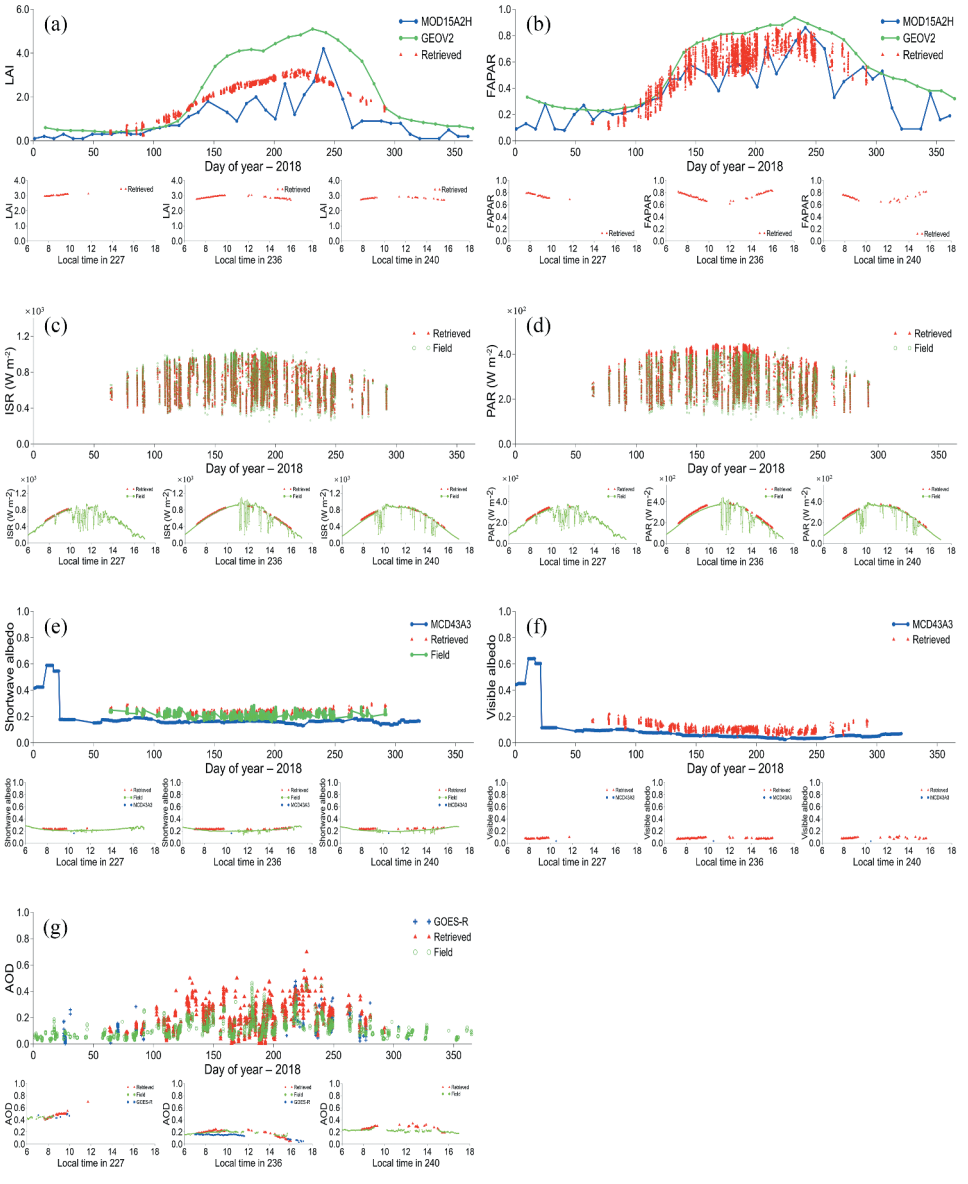

Figure 7. Time series for (*a*) LAI, (*b*) FAPAR, (*c*) ISR, (*d*) PAR, (*e*) shortwave albedo, (*f*) visible albedo, and (*g*) AOD at the Penn State site in 2018.

shortwave albedo values compared with the ground-measured shortwave albedo values. The retrieved shortwave albedo values fit well with the ground-measured shortwave albedo values, whereas the MODIS shortwave albedo values are obviously smaller than the ground-measured shortwave albedo values. Figure 7(*f*) illustrates the retrieved values and the MODIS visible albedo values. The retrieved visible albedo values are systematically higher than the MODIS visible albedo values for this site. Figure 7(*g*) demonstrates a comparison of the retrieved time-series AOD values with the GOES-R and ground-measured AOD values. The retrieved AOD values fit well with

the ground-measured AOD values. On day 236, the GOES-R AOD values are a bit lower than the retrieved and ground-measured AOD values.

Figure 8(*a*,*b*) illustrates the scatter density plots of the retrieved and GOES-R AOD values against the ground-measured AOD values. The vast majority of the retrieved AOD values demonstrate a slight overestimation of the ground-measured AOD values with the Bias of 0.047. The regression ($y = 1.223x - 0.028$) shown in Figure 8(*b*) indicates a systematic low Bias in the GOES-R AOD values with low AOD values and an opposite Bias with high AOD values. The RMSE of the retrieved AOD values (0.072) is slightly lower than that of the GOES-R AOD values (0.076) at this site. Figure 8(*c*,*d*) are scattered density plots of the retrieved ISR and PAR values against the ground measurements, respectively. The retrieved ISR values and the ground-measured ISR values achieve excellent agreement, but the retrieved PAR values were a bit overestimated evaluated with the ground-measured PAR values. Figure 8(*e*) and (*f*) are scatter density plots of the retrieved and MODIS shortwave albedo values versus the ground-measured shortwave albedo values. The retrieved shortwave albedo values perform better (RMSE = 0.029 and Bias = 0.024) against the ground-measured shortwave albedo values than the MODIS shortwave albedo values (RMSE = 0.111 and Bias = −0.051) at this site.

Figure 9 demonstrates the retrieved LAI, FAPAR, ISR, PAR, albedo, and AOD values at the Sioux Falls site in 2018. The retrieved results on days 234, 248, and 250 are also shown in Figure 9 in order to analyse intra-day variations of the retrievals. Figure 9(*a*) shows a comparison of the retrieved, GEOV2, and MODIS LAI values. Compared with the MODIS LAI values, the retrieved LAI values show consistent seasonal patterns and amplitudes. The GEOV2 LAI values are markedly higher than the retrieved and MODIS LAI values during the crop growth stage (up to 2.5 LAI units). Figure 9(*b*) shows the retrieved, GEOV2, and MODIS FAPAR values. The MODIS FAPAR values are higher than the retrieved values

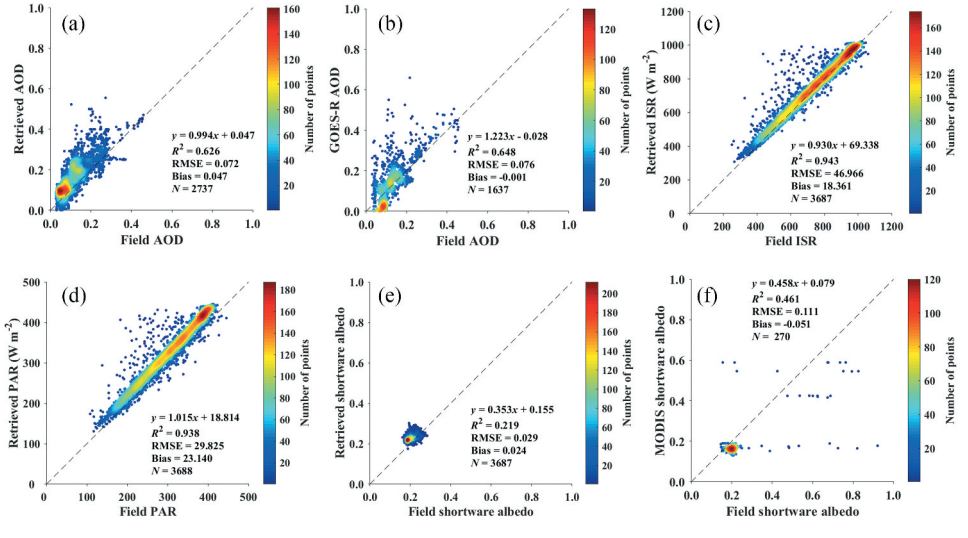

Figure 8. Scatter density plots of (*a*) the retrieved AOD values, (*b*) the GEOES-R AOD values, (*c*) the retrieved ISR values, (*d*) the retrieved PAR values, (*e*) the retrieved shortwave albedo values, and (*f*) the MODIS shortwave albedo values versus the ground measurements of the corresponding parameters at the Penn State site in 2018.

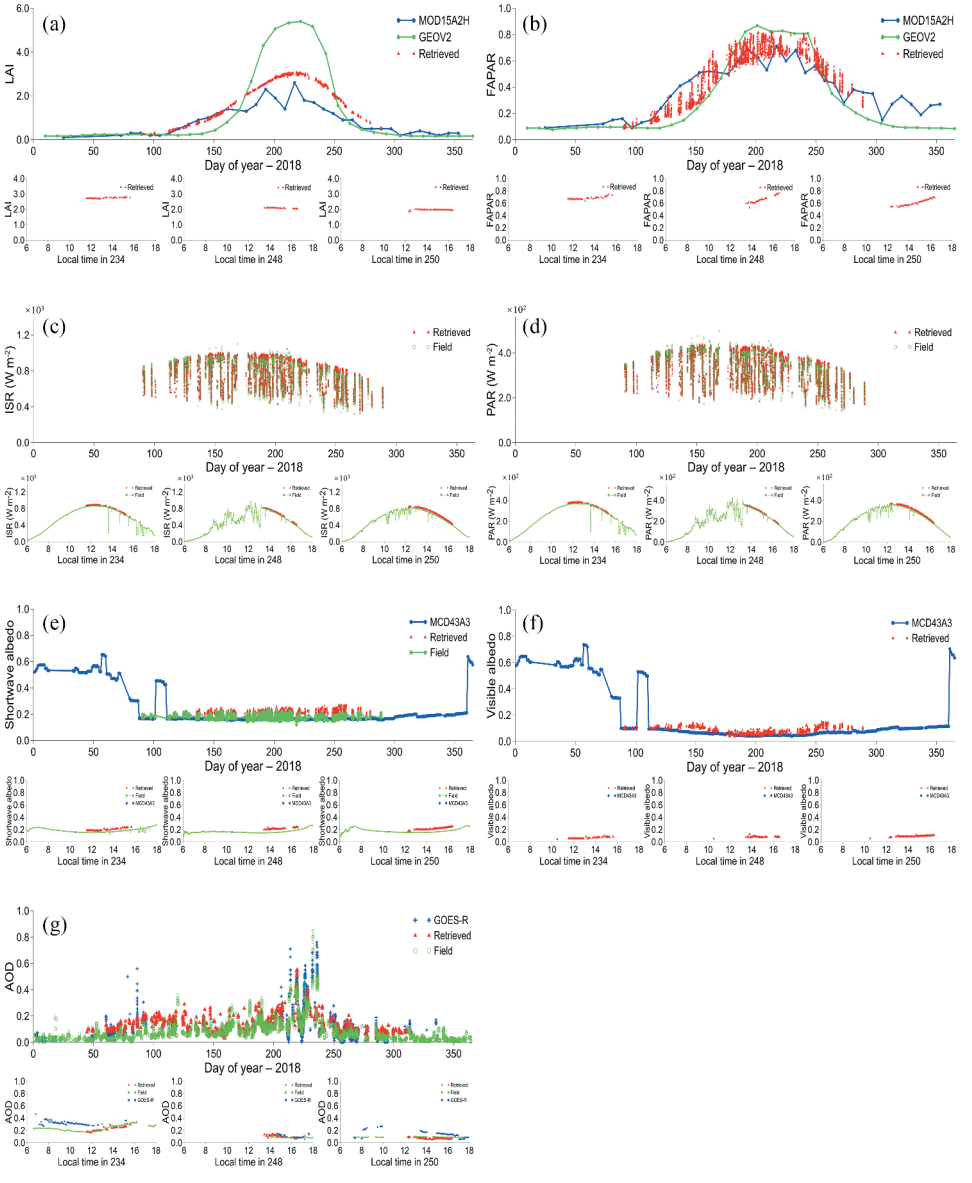

Figure 9. Time series for (*a*) LAI, (*b*) FAPAR, (*c*) ISR, (*d*) PAR, (*e*) shortwave albedo, (*f*) visible albedo, and (*g*) AOD at the Sioux Falls site in 2018.

and the GEOV2 FAPAR values outside of the time of vegetation growth stage, but the GEOV2 FAPAR values are obviously larger than the retrieved and MODIS FAPAR values during the vigorous growth stage. Obvious intra-day variations in the retrieved FAPAR profiles on days 234, 248, and 250 can be observed. The retrieved ISR and PAR values shown in Figure 9(*c*,*d*) demonstrate excellent agreement with the ground-measured ISR and PAR values at this site. Figure 9(*e*) demonstrates the retrieved shortwave albedo values, along with the MODIS and ground-measured shortwave albedo values. The retrievals fit well with the ground-measured shortwave albedo values before day 220,

but are a bit larger than the ground-measured shortwave albedo values after day 220. The MODIS visible albedo values and corresponding parameter retrievals are shown in Figure 9(*f*). Most of the retrieved visible albedo values perform well with the MODIS visible albedo values. Figure 9(*g*) illustrates that the retrieved AOD values fit well with the ground-measured AOD values, but the GOES-R AOD values are larger than the retrieved and ground-measured AOD values at this site.

Figure 10(a,b) illustrate scatter density plots of the retrieved and GOES-R AOD values versus the ground-measured AOD values, respectively. Compared with the GOES-R AOD values, the majority of the retrieved AOD values concentrated more closely at the 1:1 line versus the ground-measured AOD values. The retrieved AOD values provide a better performance (RMSE = 1.0459 and Bias = −0.5695) against the ground-measured AOD values than the GOES-R AOD values (RMSE = 1.0971 and Bias = −0.3904). Figure 10(c,d) are scatter density plots of the retrieved ISR and PAR values versus the ground-measured ISR and PAR values. The retrieved ISR and PAR values achieved fine performance with the ground-measured ISR and PAR values at this site. Figure 10(e,f) are scatter density plots of the retrieved and MODIS shortwave albedo values against the ground-measured shortwave albedo values. The retrieved and MODIS shortwave albedo values are both mainly concentrated around 0.2, with their RMSEs against the ground measurements equal to 0.304 and 0.109, respectively. It is clear that the retrieved shortwave albedo values have a better performance than the shortwave albedo values at this site.

Figure 11 illustrates the time-series of the LAI, FAPAR, ISR, PAR, albedo, and AOD values at the Table Mountain site in 2018. The retrieved parameter values on days 211, 212, and 223 are also shown in Figure 11 to analyse the intra-day variations of the retrieved parameters at this site. Figure 11(*a*) demonstrates the retrieved, GEOV2, and MODIS LAI values. The retrieved LAI values have a similar seasonal pattern to the MODIS and GEOV2 LAI values. Before day 150, the MODIS LAI values are larger than

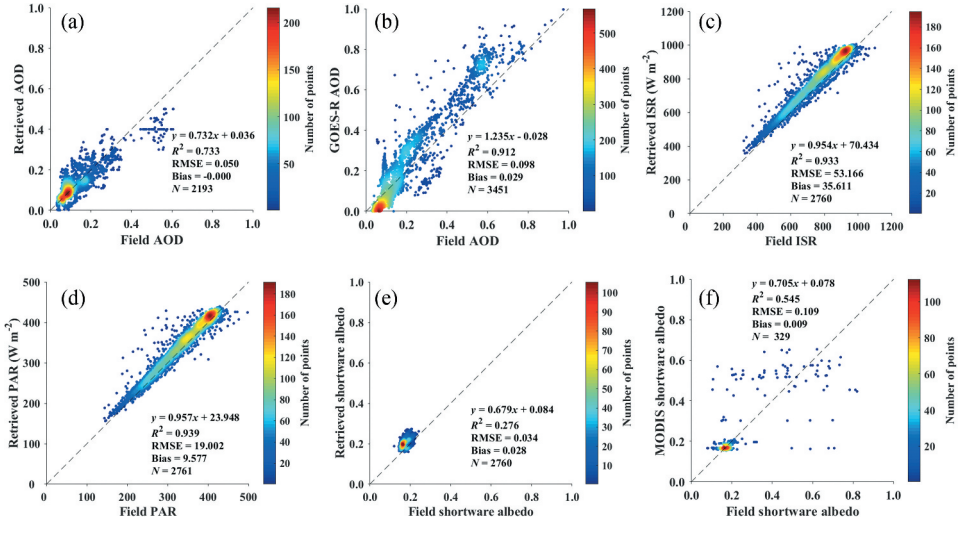

Figure 10. Scatter density plots of (*a*) the retrieved AOD values, (*b*) the GEOES-R AOD values, (*c*) the retrieved ISR values, (*d*) the retrieved PAR values, (*e*) the retrieved.

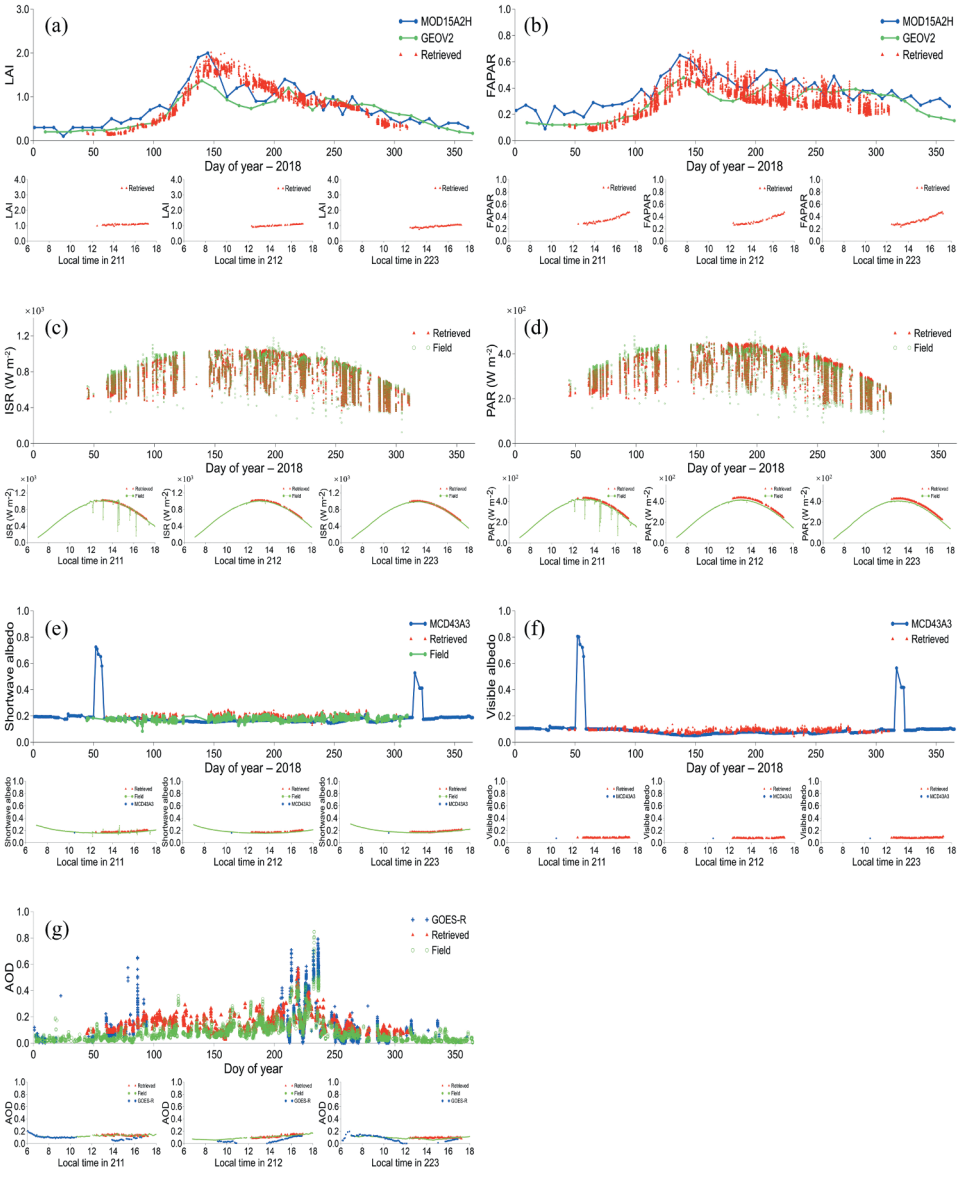

Figure 11. Time series for (*a*) LAI, (*b*) FAPAR, (*c*) ISR, (*d*) PAR, (*e*) shortwave albedo, (*f*) visible albedo, and (*g*) AOD at the Table Mountain site in 2018.

the retrieved values and the GEOV2 LAI values (up to 0.8 LAI units). Between day 150 and 200, the GEOV2 and MODIS LAI values are lower than the retrieved LAI values. The lower GEOV2 and MODIS LAI values may be caused by the cloud-contaminated satellite observations. The retrieved, GEOV2, and MODIS FAPAR values are shown in Figure 11(*b*). The retrieved FAPAR values are smaller than the GEOV2 and MODIS FAPAR values outside of the time of vegetation growth stage. Between day 150 and 200, the retrieved FAPAR values are lower than the MODIS FAPAR values but higher than the GEOV2 FAPAR values. Obvious intra-day variations of the retrieved FAPAR

values on days 211, 212, and 223 are observed. The amount of intra-day variation is more than 0.2. Figure 11(*c*) shows that the retrieved ISR values achieve outstanding agreement with the ground-measured ISR values. The retrieved PAR values shown in Figure 11(*d*) are slightly overestimated after day 170 but underestimated before that day compared with the ground-measured PAR values at this site. The retrieved values and the MODIS shortwave albedo values shown in Figure 11(*e*) demonstrated excellent agreement with the ground-measured shortwave albedo values. Moreover, the retrieved visible albedo values shown in Figure 11(*f*) are also consistent with the MODIS visible albedo values at this site. Figure 11(*g*) demonstrates that the retrieved AOD values are closer to the ground-measured AOD values than the GOES-R AOD values. The GOES-R AOD values are smaller than the ground-measured AOD values at this site.

Figure 12(a,b) illustrates the scatter density plots of the retrieved values and the GOES-R AOD values against the ground-measured AOD values, respectively. Compared with the GOES-R AOD values, the retrieved AOD values concentrated more closely at the 1:1 line versus the ground-measured AOD values. The GOES-R AOD values are in good agreement with the ground-measured AOD values for low AOD values, but overestimate the ground-measured AOD values when the AOD values were higher than 0.2. Figure 12(c,d) are scatter density plots of the retrieved ISR and PAR values against the ground-measured ISR and PAR values, respectively. The retrieved ISR and PAR values fit well with the ground measurements of the corresponding parameters at this site. Figure 12(e,f) are scatter density plots for the retrieved and MODIS shortwave albedo values versus the ground-measured shortwave albedo values, respectively. It is clear that both the retrieved and MODIS shortwave albedo values achieve excellent agreement with the ground-measured shortwave albedo values at this site.

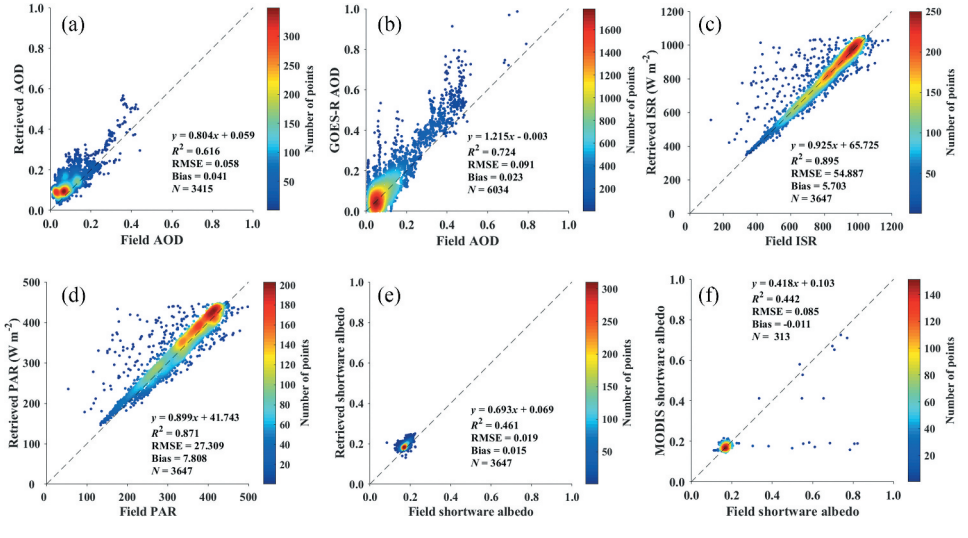

Figure 12. Scatter density plots of (*a*) the retrieved AOD values, (*b*) the GEOES-R AOD values, (*c*) the retrieved ISR values, (*d*) the retrieved PAR values, (*e*) the retrieved shortwave albedo values, and (*f*) the MODIS shortwave albedo values versus the ground measurements of the corresponding parameters at the Table Mountain site in 2018.

Table 4. Statistics of the retrieved AOD, ISR, PAR, and shortwave albedo values, the GOES-R AOD values, and the MODIS shortwave albedo values versus the ground measurements of the corresponding parameters for all five selected sites.

Site name		Bondville	Goodwin Creek	Penn State	Sioux Falls	Table Mountain	All sites
Retrieved AOD	R^2	0.471	0.689	0.626	0.733	0.616	0.567
	RMSE	0.073	0.085	0.072	0.050	0.058	0.071
	Bias	−0.007	0.064	0.047	0.000	0.041	0.034
	N	2748	4481	2737	2193	3415	15,574
GOES-R AOD	R^2	0.744	0.703	0.648	0.912	0.724	0.808
	RMSE	0.124	0.077	0.076	0.098	0.091	0.094
	Bias	0.027	−0.005	−0.001	0.029	0.023	0.015
	N	3482	5555	1637	3451	6034	20,159
Retrieved ISR	R^2	0.925	0.940	0.943	0.933	0.895	0.929
	RMSE	49.938	50.372	46.966	53.166	54.887	50.943
	Bias	18.704	20.461	18.361	35.611	5.703	19.112
	N	3881	5723	3687	2760	3647	19,698
Retrieved PAR	R^2	0.945	0.948	0.938	0.939	0.871	0.921
	RMSE	33.101	26.982	29.825	19.002	27.309	27.975
	Bias	28.803	20.006	23.140	9.577	7.808	18.607
	N	3881	5726	3688	2761	3647	19,706
Retrieved shortwave albedo	R^2	0.178	0.327	0.219	0.276	0.461	0.338
	RMSE	0.032	0.039	0.029	0.034	0.019	0.032
	Bias	0.007	0.031	0.024	0.028	0.015	0.022
	N	3881	5723	3687	2760	3647	19,698
MODIS shortwave albedo	R^2	0.650	0.021	0.461	0.545	0.442	0.512
	RMSE	0.091	0.054	0.111	0.109	0.085	0.091
	Bias	−0.017	−0.045	−0.051	0.009	−0.011	−0.023
	N	345	356	270	329	313	1613

To better evaluate the accuracy of the retrieved AOD, ISR, PAR, and shortwave albedo values, R^2, RMSE, and the Bias for each selected site are calculated and shown in Table 4. For comparison, the statistics of the GOES-R AOD values and the MODIS shortwave albedo values versus the ground measurements of the corresponding parameters are also shown in Table 4. The retrieved AOD values achieved a better performance (RMSE = 0.071) against the ground-measured AOD values compared to the GOES-R AOD values (RMSE = 0.094) for all the selected sites. The RMSE of the retrieved shortwave albedo values is 0.032, whereas the MODIS shortwave albedo values are 0.091, which illustrates that the retrieved shortwave albedo values are in better agreement with the ground-measured shortwave albedo values than the MODIS shortwave albedo values for the selected sites. The retrieved ISR and PAR values have good consistency with the ground-measured ISR and PAR values for all the selected sites. The R^2 of the retrieved ISR and PAR values are 0.929 and 0.921, respectively.

However, a positive Bias for all the selected sites indicates that the retrieved ISR, PAR, and shortwave albedo values systematically overestimated the ground-measured ISR, PAR, and shortwave albedo values, respectively. The systematic deviations may be caused by the climatic conditions, instrument calibration errors, the altitude, and the time inconsistency between measurements and retrievals (Zhang et al. 2014; Shi et al. 2017). The height of the towers selected at the SURFRAD sites is 10 m and the footprints are estimated to be about 126 m (Wang et al. 2014), which differs from the retrievals on a spatial scale. This may somehow lead to slight errors despite the fact that the sites are spatially representative during the growing season.

4. Conclusions and discussion

Current remote sensing products are mainly generated from polar-orbiting satellite data, which are not sufficient for studying intra-day variations of parameters, such as surface albedo, FAPAR, and ISR. Moreover, these parameter products are generally produced by parameter-specific algorithms, which leads to physical inconsistency among different parameters.

In this study, a new method for multi-parameter consistent estimation from geostationary satellite data is proposed. It was applied to simultaneously retrieve AOD, LAI, ISR, PAR, FAPAR, and surface albedo from GOES-R TOA reflectance data. The spatial and temporal resolutions of the retrieved parameters are 1 km and up to 5 minutes, respectively. Validations of the retrieved parameter values versus ground measurements were conducted across five sites with different vegetation types. The results illustrate that the retrieved AOD, PAR, ISR, and surface albedo values have consistent intra-day variations with the ground measurements, and the retrieved parameter values performed well versus the ground measurements for all the selected sites.

However, there are still some problems in this study. The first issue is that there are no ground-measured LAI, FAPAR, and visible albedo at the selected SURFRAD sites. This study evaluates them by making a comparison with existing satellite products. The validation of these parameters will be focused on future work if field measurements become available. The second issue is that the 6 S radiative transfer model can be only used under clear-sky conditions; thus, the cloudy observations are not used in this study. The radiative transfer models that can take cloudy conditions into account such as MODTRAN or libRadtran will be tested. In addition, this paper only uses GOES-R TOA reflectance. Estimating parameters from TOA reflectance data acquired by other geostationary satellite such as Himawari-8 and FY-4A will also be tested in the future.

Acknowledgements

The authors want to express their thanks to SURFRAD for providing ground measurements data, and NOAA for providing the GOES-R data.

Disclosure statement

No potential conflict of interest was reported by the authors.

Funding

This work was supported by the National Natural Science Foundation of China [41771359].

References

Augustine, J. A., J. J. DeLuisi, and C. N. Long. 2000. "SURFRAD–A National Surface Radiation Budget Network for Atmospheric Research." *Bulletin of the American Meteorological Society* 81 (10): 2341–2358. doi:10.1175/1520-0477(2000)081<2341:Sansrb>2.3.Co;2.

Baret, F., M. Weiss, R. Lacaze, F. Camacho, H. Makhmara, P. Pacholcyzk, and B. Smets. 2013. "GEOV1: LAI and FAPAR Essential Climate Variables and FCOVER Global Time Series Capitalizing over

Existing Products. Part1: Principles of Development and Production." *Remote Sensing of Environment* 137: 299–309. doi:10.1016/j.rse.2012.12.027.

Baret, F., O. Hagolle, B. Geiger, P. Bicheron, B. Miras, M. Huc, B. Berthelot, et al. 2007. "LAI, fAPAR and fCover CYCLOPES Global Products Derived from VEGETATION." *Remote Sensing of Environment* 110 (3): 275–286. doi:10.1016/j.rse.2007.02.018.

Bessho, K., K. Date, M. Hayashi, A. Ikeda, T. Imai, H. Inoue, Y. Kumagai, et al. 2016. "An Introduction to Himawari-8/9— Japan's New-Generation Geostationary Meteorological Satellites." *Journal of the Meteorological Society of Japan. Ser. II* 94 (2): 151–183. doi:10.2151/jmsj.2016-009.

Claverie, M., E. Vermote, and N. O. A. A. C. D. R. Program. 2014. "NOAA Climate Data Record (CDR) of Leaf Area Index (LAI) and Fraction of Absorbed Photosynthetically Active Radiation (FAPAR)", Version 4." *NOAA National Climatic Data Center*. doi:10.7289/V5M043BX.

Collow, A. B. M., S. P. Mahanama, M. G. Bosilovich, R. D. Koster, and S. D. Schubert 2017. "An Evaluation of Teleconnections over the United States in an Ensemble of AMIP Simulations with the MERRA-2 Configuration of the GEOS Atmospheric Model, Technical Report Series on Global Modeling and Data Assimilation." *NASA/TM-2017-104606, Greenbelt, Maryland*. https://ntrs.nasa.gov/search.jsp?R=20180001607

Dong, T., W. Bingfang, J. Meng, X. Du, and J. Shang. 2016. "Sensitivity Analysis of Retrieving Fraction of Absorbed Photosynthetically Active Radiation (FPAR) Using Remote Sensing Data." *Acta Ecologica Sinica* 36 (1): 1–7. doi:10.1016/j.chnaes.2015.12.003.

Dong, Y., Z. Jiao, S. Yin, H. Zhang, X. Zhang, L. Cui, H. Dandan, A. Ding, Y. Chang, and S. Yang. 2018. "Influence of Snow on the Magnitude and Seasonal Variation of the Clumping Index Retrieved from MODIS BRDF Products." *Remote Sensing* 10 (8): 1194. doi:10.3390/rs10081194.

Duan, Q. Y., V. K. Gupta, and S. J. Sorooshian. 1993. "Shuffled Complex Evolution Approach for Effective and Efficient Global Minimization." *The Journal of Optimization Theory and Applications* 76 (3): 501. doi:10.1007/BF00939380.

Henry, P., T. Gentet, M. Arnaud, and C. Andersson. 1996. "THe VEGETATION System: A Global Earth Monitoring from SPOT Satellites." *Acta astronautica* 38 (4): 487–492. doi:10.1016/0094-5765(96)00019-7.

Jacquemoud, S., and F. Baret. 1990. "PROSPECT: A Model of Leaf Optical Properties Spectra." *Remote Sensing of Environment* 34 (2): 75–91. doi:10.1016/0034-4257(90)90100-Z.

Jiang, Z., A. Huete, K. Didan, and T. Miura. 2008. "Development of a Two-band Enhanced Vegetation Index without a Blue Band." *Remote Sensing of Environment* 112 (10): 3833–3845. doi:10.1016/j.rse.2008.06.006.

Jiao, Z., Y. Dong, C. B. Schaaf, J. M. Chen, M. Román, Z. Wang, H. Zhang, et al. 2018. "An Algorithm for the Retrieval of the Clumping Index (CI) from the MODIS BRDF Product Using an Adjusted Version of the Kernel-driven BRDF Model." *Remote Sensing of Environment* 209:594–611. doi:10.1016/j.rse.2018.02.041.

Jiao, Z., M. J. Hill, C. B. Schaaf, H. Zhang, Z. Wang, and L. Xiaowen. 2014. "An Anisotropic Flat Index (AFX) to Derive BRDF Archetypes from MODIS." *Remote Sensing of Environment* 2014 (v.141): 168–187. doi:10.1016/j.rse.2013.10.017.

Jiao, Z., C. B. Schaaf, Y. Dong, M. Román, M. J. Hill, J. M. Chen, Z. Wang, et al. 2016. "A Method for Improving Hotspot Directional Signatures in BRDF Models Used for MODIS." *Remote Sensing of Environment* 186 :135–151. doi:10.1016/j.rse.2016.08.007.

Kaufman, Y. J., D. Tanré, L. A. Remer, E. F. Vermote, A. Chu, and B. N. Holben. 1997. "Operational Remote Sensing of Tropospheric Aerosol over Land from EOS Moderate Resolution Imaging Spectroradiometer." *Journal of Geophysical Research Atmospheres* 102 (D14): 17051–17067. doi:10.1029/96JD03988.

Kim, M., J. Kim, O. Torres, C. Ahn, W. Kim, U. Jeong, G. Sujung, X. Liu, K. Moon, and D.-R. Kim. 2018. "Optimal Estimation-Based Algorithm to Retrieve Aerosol Optical Properties for GEMS Measurements over Asia." *Remote Sensing* 10 (2): 2. doi:10.3390/rs10020162.

Kuusk, A. 2001. "A Two-layer Canopy Reflectance Model." *Journal of Quantitative Spectroscopy & Radiative Transfer* 71 (1): 1–9. doi:10.1016/S0022-4073(01)00007-3.

Lauvernet, C., F. Baret, L. Hascoët, S. Buis, and F.-X. Le Dimet. 2008. "Multitemporal-patch Ensemble Inversion of Coupled Surface–atmosphere Radiative Transfer Models for Land Surface Characterization." *Remote Sensing of Environment* 112 (3): 851–861. doi:10.1016/j.rse.2007.06.027.

Lee, J., J. Kim, C. H. Song, J.-H. Ryu, Y.-H. Ahn, and C. K. Song. 2010. "Algorithm for Retrieval of Aerosol Optical Properties over the Ocean from the Geostationary Ocean Color Imager." *Remote Sensing of Environment* 114 (5): 1077–1088. doi:10.1016/j.rse.2009.12.021.

Liang, S., X. Zhao, S. Liu, W. Yuan, X. Cheng, Z. Xiao, X. Zhang, et al. 2013. "A Long-term Global LAnd Surface Satellite (GLASS) Data-set for Environmental Studies." *International Journal of Digital Earth* 6 (sup1): 5–33. doi:10.1080/17538947.2013.805262.

Long, C. N., and T. P. Ackerman. 2000. "Identification of Clear Skies from Broadband Pyranometer Measurements and Calculation of Downwelling Shortwave Cloud Effects." *Journal of Geophysical Research: Atmospheres* 105 (D12): 15609–15626. doi:10.1029/2000jd900077.

Mei, L., Y. Xue, G. de Leeuw, T. Holzer-Popp, J. Guang, Y. Li, L. Yang, et al. 2012. "Retrieval of Aerosol Optical Depth over Land Based on a Time Series Technique Using MSG/SERIVI Data." *Atmospheric Chemistry and Physics Discussions* 12 (2): 4031–4071. doi:10.5194/acpd-12-4031-2012.

Pinter, P. J. 1993. "Solar Angle Independence in the Relationship between Absorbed PAR and Remotely Sensed Data for Alfalfa." *Remote Sensing of Environment* 46 (1): 19–25. doi:10.1016/0034-4257(93)90029-W.

Salomonson, V. V., W. L. Barnes, P. W. Maymon, H. E. Montgomery, and H. Ostrow. 1989. "MODIS: Advanced Facility Instrument for Studies of the Earth as a System." *IEEE Transactions on Geoscience and Remote Sensing* 27 (2): 145–153. doi:10.1109/36.20292.

Schaaf, C., and Z. Wang. 2015. "MCD43A3 MODIS/Terra+Aqua BRDF/Albedo Daily L3 Global - 500m V006." *NASA EOSDIS Land Processes DAAC*. doi:10.5067/MODIS/MCD43A3.006.

Schmit, T. J., L. Jun, L. Jinlong, W. F. Feltz, J. J. Gurka, M. D. Goldberg, and K. J. Schrab. 2008. "The GOES-R Advanced Baseline Imager and the Continuation of Current Sounder Products." *Journal of Applied Meteorology and Climatology* 47 (10): 2696–2711. doi:10.1175/2008jamc1858.1.

Shi, H., Z. Xiao, S. Liang, and H. Ma. 2017. "A Method for Consistent Estimation of Multiple Land Surface Parameters from MODIS Top of Atmosphere Time Series Data." *IEEE Transactions on Geoscience and Remote Sensing* 55 (9): 5158–5173. doi:10.1109/TGRS.2017.2702609.

Shi, H., Z. Xiao, S. Liang, and X. Zhang. 2016. "Consistent Estimation of Multiple Parameters from MODIS Top of Atmosphere Reflectance Data Using a Coupled Soil-canopy-atmosphere Radiative Transfer Model." *Remote Sensing of Environment* 184: 40–57. doi:10.1016/j.rse.2016.06.008.

Shi, S., T. Cheng, G. Xingfa, H. Letu, H. Guo, H. Chen, Y. Wang, and W. Yu. 2018. "Synergistic Retrieval of Multitemporal Aerosol Optical Depth over North China Plain Using Geostationary Satellite Data of Himawari-8." *Journal of Geophysical Research: Atmospheres* 123 (10): 5525–5537. doi:10.1029/2017jd027963.

Townshend, J. R. G. 2007. "Global Data Sets for Land Applications from the Advanced Very High Resolution Radiometer: An Introduction." *International Journal of Remote Sensing* 15 (17): 3319–3332. doi:10.1080/01431169408954333.

Valenti, J., NOAA. 2018. "GOES-R Ground Segment Project Manager. GOES-R Product Definition and Users' Guide." Vol. 3, Rev. 2.0. https://www.goes-r.gov/users/docs/PUG-L1b-vol3.pdf

Verhoef, W. 1985. "Earth Observation Modeling Based on Layer Scattering Matrices." *Remote Sensing of Environment* 17 (2): 165–178. doi:10.1016/0034-4257(85)90072-0.

Verhoef, W., and H. Bach. 2003. "Simulation of Hyperspectral and Directional Radiance Images Using Coupled Biophysical and Atmospheric Radiative Transfer Models." *Remote Sensing of Environment* 87 (1): 23–41. doi:10.1016/s0034-4257(03)00143-3.

Verhoef, W., and H. Bach. 2007. "Coupled Soil–leaf-canopy and Atmosphere Radiative Transfer Modeling to Simulate Hyperspectral Multi-angular Surface Reflectance and TOA Radiance Data." *Remote Sensing of Environment* 109 (2): 166–182. doi:10.1016/j.rse.2006.12.013.

Vermote, E. F., D. Tanré, J. L. Deuzé, M. Herman, -J.-J. Morcrette, and S. Y. Kotchenova 2006. "6S User Guide Version 3"

Walthall, C. L., J. M. Norman, J. M. Welles, G. Campbell, and B. L. Blad. 1985. "Simple Equation to Approximate the Bidirectional Reflectance from Vegetative Canopies and Bare Soil Surfaces." *Applied Optics* 24 (3): 383–387. doi:10.1364/AO.24.000383.

Wang, Z., C. B. Schaaf, A. H. Strahler, M. J. Chopping, M. O. Román, Y. Shuai, C. E. Woodcock, D. Y. Hollinger, and D. R. Fitzjarrald. 2014. "Evaluation of MODIS Albedo Product (MCD43A) over Grassland, Agriculture and Forest Surface Types during Dormant and Snow-covered Periods." *Remote Sensing of Environment* 140: 60–77. doi:10.1016/j.rse.2013.08.025.

Xiao, Z., S. Liang, J. Wang, P. Chen, X. Yin, L. Zhang, and J. Song. 2014. "Use of General Regression Neural Networks for Generating the GLASS Leaf Area Index Product from Time-Series MODIS Surface Reflectance." *IEEE Transactions on Geoscience and Remote Sensing* 52 (1): 209–223. doi:10.1109/tgrs.2013.2237780.

Xiao, Z., S. Liang, J. Wang, B. Jiang, and L. Xijia. 2011. "Real-time Retrieval of Leaf Area Index from MODIS Time Series Data." *Remote Sensing of Environment* 115 (1): 97–106. doi:10.1016/j.rse.2010.08.009.

Xiao, Z., S. Liang, J. Wang, Y. Xiang, X. Zhao, and J. Song. 2016. "Long-Time-Series Global Land Surface Satellite Leaf Area Index Product Derived from MODIS and AVHRR Surface Reflectance." *IEEE Transactions on Geoscience and Remote Sensing* 54 (9): 5301–5318. doi:10.1109/tgrs.2016.2560522.

Xiao, Z., S. Liang, J. Wang, D. Xie, J. Song, and R. Fensholt. 2015. "A Framework for Consistent Estimation of Leaf Area Index, Fraction of Absorbed Photosynthetically Active Radiation, and Surface Albedo from MODIS Time-Series Data." *IEEE Transactions on Geoscience and Remote Sensing* 53 (6): 3178–3197. doi:10.1109/tgrs.2014.2370071.

Zhang, H., R. M. Hoff, S. Kondragunta, I. Laszlo, and A. Lyapustin. 2013. "Aerosol Optical Depth (AOD) Retrieval Using Simultaneous GOES-East and GOES-West Reflected Radiances over the Western United States." *Atmospheric Measurement Techniques* 6 (2): 471–486. doi:10.5194/amt-6-471-2013.

Zhang, H., A. Lyapustin, Y. Wang, S. Kondragunta, I. Laszlo, P. Ciren, and R. M. Hoff. 2011. "A Multi-angle Aerosol Optical Depth Retrieval Algorithm for Geostationary Satellite Data over the United States." *Atmospheric Chemistry and Physics* 11 (23): 11977–11991. doi:10.5194/acp-11-11977-2011.

Zhang, W., X. Hui, and F. Zheng. 2018. "Aerosol Optical Depth Retrieval over East Asia Using Himawari-8/AHI Data." *Remote Sensing* 10: 1. doi:10.3390/rs10010137.

Zhang, X., S. Liang, G. Zhou, W. Haoran, and X. Zhao. 2014. "Generating Global LAnd Surface Satellite Incident Shortwave Radiation and Photosynthetically Active Radiation Products from Multiple Satellite Data." *Remote Sensing of Environment* 152: 318–332. doi:10.1016/j.rse.2014.07.003.

Zhu, Z., B. Jian, Y. Pan, S. Ganguly, A. Anav, X. Liang, A. Samanta, S. Piao, R. Nemani, and R. Myneni. 2013. "Global Data Sets of Vegetation Leaf Area Index (Lai)3g and Fraction of Photosynthetically Active Radiation (Fpar)3g Derived from Global Inventory Modeling and Mapping Studies (GIMMS) Normalized Difference Vegetation Index (Ndvi3g) for the Period 1981 to 2011." *Remote Sensing* 5 (2): 927–948. doi:10.3390/rs5020927.